

PROCEEDINGS OF SPIE

SPIDigitalLibrary.org/conference-proceedings-of-spie

Mosaic microtomography of a full mouse brain with sub-micron pixel size

Griffin Rodgers, Christine Tanner, Georg Schulz, Timm Weitkamp, Mario Scheel, et al.

Griffin Rodgers, Christine Tanner, Georg Schulz, Timm Weitkamp, Mario Scheel, Marta Girona Alarcón, Vartan Kurtcuoglu, Bert Müller, "Mosaic microtomography of a full mouse brain with sub-micron pixel size," Proc. SPIE 12242, Developments in X-Ray Tomography XIV, 122421L (14 October 2022); doi: 10.1117/12.2633556

SPIE.

Event: SPIE Optical Engineering + Applications, 2022, San Diego, California, United States

Mosaic microtomography of a full mouse brain with sub-micron pixel size

Griffin Rodgers^{*a,b}, Christine Tanner^{*a,b}, Georg Schulz^{a,b,c}, Timm Weitkamp^d, Mario Scheel^d, Marta Girona Alarcón^e, Vartan Kurtcuoglu^{e,f}, and Bert Müller^{*a,b}

^aBiomaterials Science Center, Department of Biomedical Engineering, University of Basel, 4123 Allschwil, Switzerland

^bBiomaterials Science Center, Department of Clinical Research, University Hospital Basel, 4031 Basel, Switzerland

^cCore Facility Micro- and Nanotomography, Department of Biomedical Engineering, University of Basel, 14, 4123 Allschwil, Switzerland

^dSynchrotron SOLEIL, 91190 Saint-Aubin, France

^eThe Interface Group, Institute of Physiology, University of Zurich, 8057 Zurich, Switzerland

^fNational Centre of Competence in Research, Kidney.CH, 8057 Zurich, Switzerland

ABSTRACT

Mammalian brains are extremely complex: a mouse brain contains one hundred million neurons. Mapping an entire brain's three-dimensional cytoarchitecture from the nano- to centimeter-scale is a monumental challenge. For standard microtomography with sub- μm pixel size, reconstructed volume is limited to about a few mm^3 . For full brain mapping, even for the mouse brain with volume of 450 mm^3 , the field-of-view must be significantly increased in all three dimensions. We demonstrate mosaic tiling to extend imaged volume by $400\times$ and a dedicated pipeline to process these tera-voxel sized datasets. Here, an entire mouse brain was imaged with $0.65 \mu\text{m}$ -wide voxels. The datasets, which are 6 TB in size at 16-bit depth, contain a wealth of microanatomical information but present challenges for registration and segmentation.

Keywords: X-ray virtual histology, field-of-view, hierarchical imaging, mosaic, mouse brain, synchrotron radiation, brain atlas, neuroimaging

1. INTRODUCTION

Neuroimaging is critical for decoding the brain's structure-function relationship.¹ However, even for smaller mammals such as mice, comprehensive brain mapping requires imaging over multiple orders of magnitude. For example, the width of the entire mouse brain is on the order of 10 mm, the size of cells is typically on the order of μm , synaptic connections can be thinner than 100 nm, and morphological changes on the order of a few nm can affect brain circuit function.¹ Therefore, a combination of imaging techniques are used to visualize the three-dimensional cytoarchitecture of the brain. Among these, virtual histology based on X-ray microtomography holds promise as a *post mortem* modality that can provide volumetric brain imaging with isotropic μm resolution.²⁻⁶ However, current results mostly explore brain volumes on the order of tens of mm^3 , while the volume of the mouse brain is around 450 mm^3 .⁷ Thus, the extension of microtomography for full-brain mapping has generated considerable interest in recent years.⁸⁻¹²

While hard X-ray penetration of soft tissues theoretically allows for microtomography of entire centimeter-sized brains, the field-of-view (FOV) is typically limited by detector array size. Standard detector arrays consist of a few thousand pixels in each direction, e.g. the Hamamatsu Orca Flash 4.0 V2 currently employed at the ANATOMIX beamline of Synchrotron SOLEIL^{13,14} consists of a 2048×2048 array of $6.5 \mu\text{m}$ -wide pixels. Using $10\times$ magnification and a single detector FOV, $0.65 \mu\text{m}$ pixel size and down to $1.5 \mu\text{m}$ resolution can be achieved

*Send correspondence to G.R., e-mail: griffin.rodgers@unibas.ch, C.T., email: christine.tanner@unibas.ch, and B.M., email: bert.mueller@unibas.ch, telephone: +41 61 207 54 38, www.bmc.unibas.ch

with FOV of $1.3 \times 1.3 \times 1.3 \text{ mm}^3$. Such a local tomography scan already holds rich microanatomical information, see Figure 1. An off-axis acquisition can extend reconstructed volume to $2.5 \times 2.5 \times 1.3 \text{ mm}^3$. Still, the volume of the mouse brain is about $200\times$ larger, therefore the FOV must be significantly extended for brain mapping.

Translation of the sample along the axis of rotation allows for extension of FOV *via* helical scans or, more commonly, stitching reconstructions from several height steps. Extending the FOV orthogonal to the rotation axis can be accomplished by either stitching reconstructions of local tomography scans^{15,16} or building mosaic projections with a common center-of-rotation (COR) prior to reconstruction.^{8,17} The former allows for standard reconstruction provided by most microtomography beamlines, though corrections are needed for well-known local tomography artefacts from truncated sinograms^{18–20} and dedicated software for non-rigid stitching is required if the sample is deformed during acquisition.¹⁶ The latter is considered to be more dose- and time-efficient,⁹ though it requires a dedicated pipeline for mosaic stitching of projections and reconstruction of large datasets.^{8,11,17}

This work presents the development of a custom reconstruction pipeline for mosaic-style tomographic reconstruction of entire organs with cellular resolution. Here, we discuss data acquisition, data treatment, and implementation of this reconstruction pipeline. Finally, we demonstrate the reconstruction of the entire mouse brain with $0.65 \mu\text{m}$ -wide voxels.

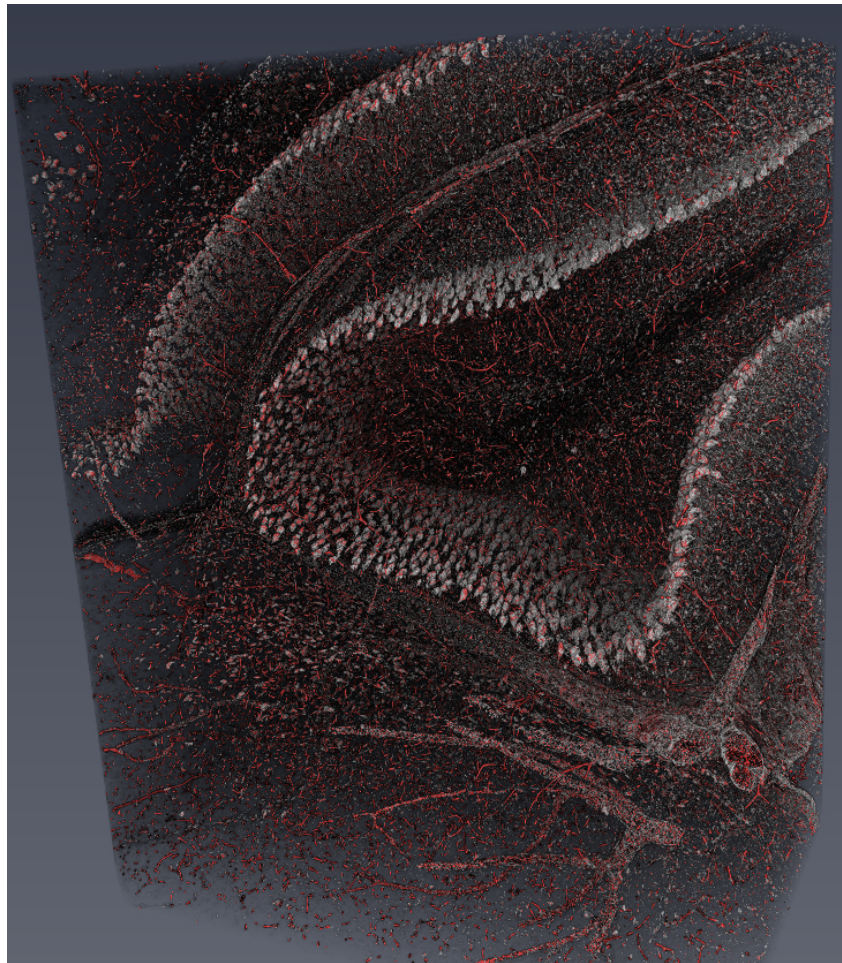


Figure 1. Volume rendering of a local tomography scan with $0.65 \mu\text{m}$ -wide voxels within the cerebellum of a formalin-fixed mouse brain. The Purkinje cell layer (gray, cells are about $10 \mu\text{m}$ in width) as well as the vasculature (red) are clearly visible. The rendering represents a cropped field-of-view of approximately 1 mm^3 , while the volume of the entire mouse brain is around 450 mm^3 . Measurements were performed at the ANATOMIX Beamline^{13,14} of Synchrotron SOLEIL (Saint-Aubin, France). The volume rendering was made with Amira 6.2.0 (Thermo Fisher Scientific Inc., Waltham, USA).

2. MATERIALS AND METHODS

2.1 Animals and tissue preparation

The brain of a one-year-old female C57BL/6JRj mouse (Janvier Labs, Le Genest-Saint-Isle, France) was extracted and transcardially perfused with 4% formaldehyde / phosphate buffered saline after sacrifice, then immersed in 4% formaldehyde / phosphate buffered saline. The mouse brain collected for this study was excess from an experiment approved by the veterinary office of the Canton of Zurich (license number ZH067/17). For ethanol dehydration, the brain was immersed for two hours in 20 mL of each of 50%, 70%, 80%, 90%, and 100% ethanol (Carl Roth GmbH, Karlsruhe, Germany). The brain was measured in 100% ethanol to take advantage of enhanced contrast from ethanol dehydration.^{21–23}

2.2 Extended-field microtomography acquisition

Imaging was performed at the ANATOMIX beamline at Synchrotron SOLEIL (Saint-Aubin, France).^{13,14} A filtered white beam with effective mean photon energy of around 27 keV was attained by setting the undulator gap to 5.5 mm and inserting 20 μm Au and 100 μm Cu filters into the beam path. The detector consisted of a 20 μm -thick LuAG scintillator coupled to a scientific CMOS camera (Hamamatsu Orca Flash 4.0 V2, 2048 \times 2048 pixels, 6.5 μm physical pixel size) *via* a Mitutoyo (Mitutoyo Europe GmbH, Neuss, Germany) microscope objective (10 \times , NA 0.28) resulting in a magnification factor of 10 and an effective pixel size of 0.65 μm .²⁴ The detector was placed 50 mm downstream of the sample for single-distance phase retrieval. This distance was selected based on $z_c = (2\Delta)^2/\lambda$ with pixel size Δ and wavelength λ to ensure that blurring from propagation-based phase contrast does not exceed two pixels.²⁵ The exposure time was set to 100 ms to fill half of the detector's dynamic range, which reduces severity of ring artefacts.

To cover the full width of the mouse brain, the detector's FOV had to be linearly extended by a factor of 8, which corresponds to a 64 \times larger reconstructed area. This was achieved with the acquisition of 4 rings, each consisting of a 360 $^\circ$ scan with offset COR, see Figure 2. The COR was offset by 0.6, 1.8, 3.0, and 4.2 mm for rings 1, 2, 3, and 4, respectively. Note that in this convention, 0 mm corresponds to the COR at the center of the detector FOV. Each ring scan consisted of 9000 projections. The acquisition of each ring took around 15 minutes, as a fly scan mode was used. Note that precise tilt alignment of the rotation stage is critical, as a reconstructed slice is 0.65 μm thick and 10 mm wide.

A total of 8 height steps were needed to cover the mouse brain from cerebellum to olfactory bulbs. Height steps were acquired with offset of 1.2 mm, corresponding to an overlap of about 200 pixels. The total scan time was slightly over 8 hours.

2.3 Reconstruction of mosaic-style tomography data

The reconstruction pipeline had four main steps: (i) determination of the COR and ring overlap positions; (ii) projection blending, ring artefact correction, and filtering for phase retrieval and/or noise reduction; (iii) tomographic reconstruction; and (iv) blending of height steps. These steps are laid out in greater detail in the following sections. The pipeline was built around a parameter file that contained information on the sample name, filtering, ring correction, output grayscale, and cropping options. This parameter file was accompanied by a table containing file paths to the raw data of the component ring scans. Each step of the pipeline could be launched with only the parameter file as an input and was designed to run as batch jobs on either standard workstations or scientific computing infrastructure, e.g. with [sciCORE](#) at the University of Basel. Note that this reconstruction pipeline was not the one in use at ANATOMIX, which provided options for standard and off-axis reconstructions.

2.3.1 Center-of-rotation and overlap positions

The COR was found by maximizing cross-correlation in overlapping regions of projection pairs from the inner ring with rotation angles 180 $^\circ$ apart. The mouse brain sample had relatively low contrast in projections, therefore 10 flat-field corrected projection pairs were used to increase robustness. Peaks in the cross-correlation curves were automatically identified and their prominence determined with the `Matlab` function `findpeaks`. The COR was selected from the prominence-weighted average positions of these peaks. Overlap positions between rings and

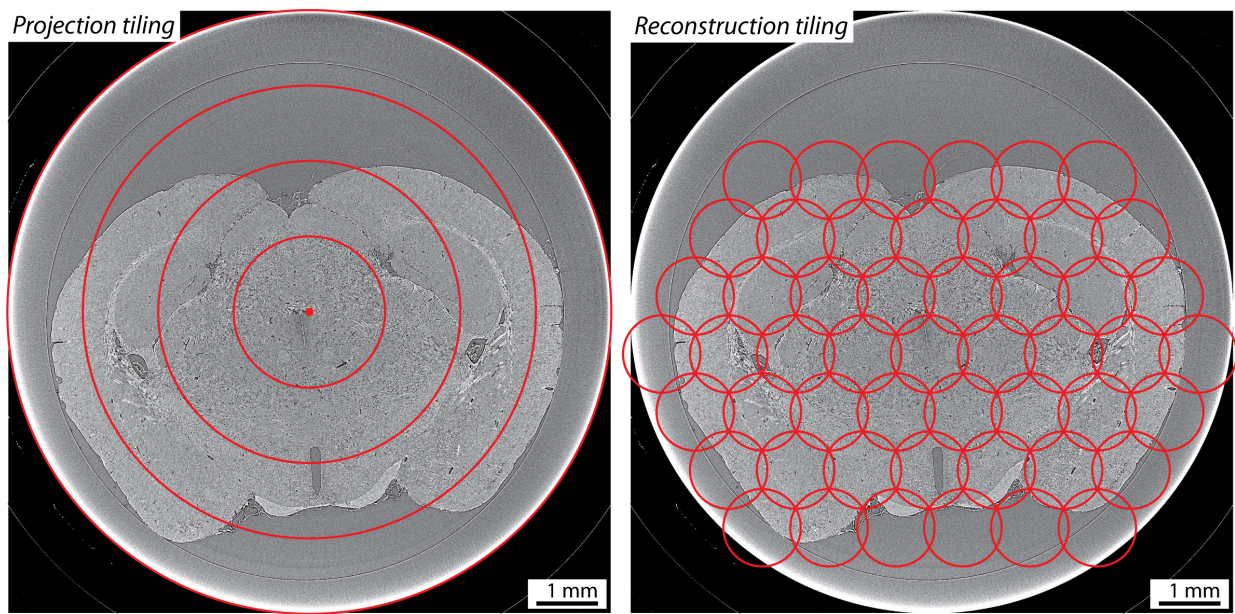
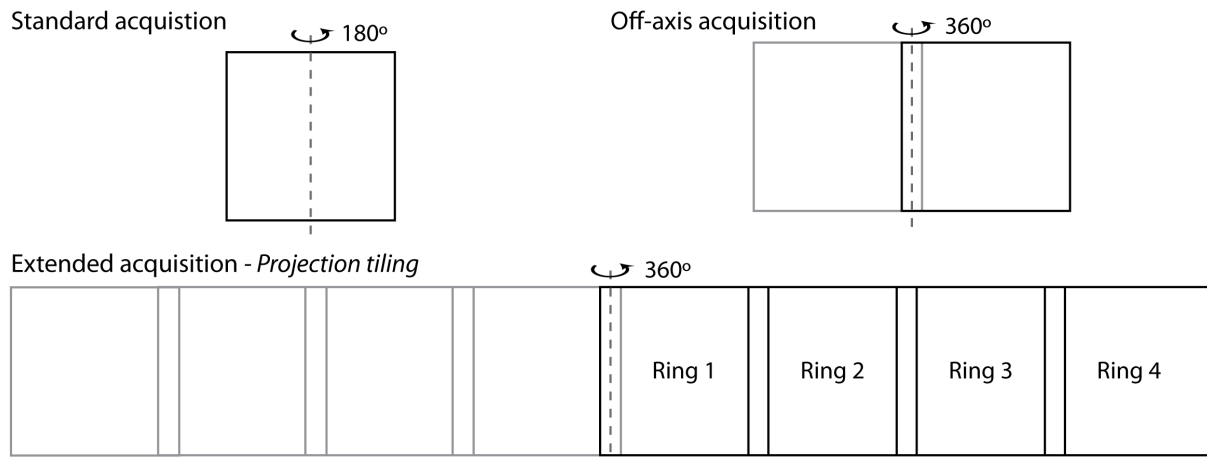


Figure 2. Acquisition for large FOV microtomography. Conventionally, microtomography scans rely on acquisition of one (top left) or two detector FOV's (top right). FOV can be extended perpendicular to the rotation axis by acquiring projections in concentric rings (middle). Microtomography of a full mouse brain with 0.65 μm -wide voxels is illustrated for projection or reconstruction tiling (bottom, left and right, respectively). The full coronal cross-sectional area of the mouse brain can be imaged by stitching 4 offset center-of-rotation projection "rings" before reconstruction (bottom left). Alternatively, local tomography scans with FOV given by a single detector FOV can be stitched together after reconstruction – approximately 50 local scans (or about 16 off-axis scans) are needed for one height step of the mouse brain (bottom right).

height steps were also found by maximizing cross-correlation in overlapping regions of projections from adjacent acquisitions. Again, prominence-weighted average peak positions from 10 flat-field corrected projection pairs were used to increase robustness. The recorded motor position of the translation stage were used as an initial estimate to limit the search range for both COR and overlap positions between rings. The output of this step of the pipeline was a list of overlap positions that can be used to build mosaic projections.

2.3.2 Projection blending, ring artefact correction, and filtering of radiographic projections

The next step generated large FOV mosaic projections. Single FOV projections were flat-field corrected and then combined with linear blending, i.e. $I_{\text{blend}} = \alpha I_r + (1 - \alpha)I_{r+1}$ with $\alpha \in [0, 1]$ linearly increasing through

the overlap region, to create 8×8 extended mosaic projections around 180° of rotation. After blending, phase retrieval was performed using Paganin's filter.²⁶

Ring artefacts were severe if no additional correction was applied. The correction used for the mouse brain dataset was based on the mean of flat-field corrected projections over all rotation angles. This mean projection contained spot-like features that were the result of inhomogeneities that remained in fixed positions on the detector during acquisition. These inhomogeneities, which may have been caused by detector non-linearity, were the source of ring artefacts because they could not be fully removed by flat-field correction. The mean projection was high-pass filtered to isolate the ring artefact sources and subtracted from all projections prior to reconstruction.

It is critical to select suitable parameters for both ring correction and filtering *before* reconstruction of teravoxel-sized datasets. Previews were generated relatively quickly by processing projections covering the full sample width but cropped in height to a stripe of e.g. 32 pixels. This allowed for selection of the desired high-pass filter for the mean projection to be used for ring correction as well as the δ/β ratio in Paganin's phase retrieval.²⁶ For this mouse brain, a ratio of $\delta/\beta = 200$ was chosen based on visual inspection of the reconstructions, considering the trade-off between contrast and spatial resolution.²⁷

The flat-field corrected, filtered, and blended projections were written to image files to be accessed for reconstruction. The full mouse brain consisted of 4495 projections 14982×14982 in size, resulting in a data size of about $4495 \times 900 \text{ MB} = 4 \text{ TB}$ at 32-bit precision prior to reconstruction. The projections were saved as TIFFs with tiling such that 14982×32 strips could be quickly read for block-wise reconstruction.

2.3.3 Tomographic reconstruction

Reconstruction was performed on blocks of 32 sinograms to avoid excessive memory consumption and allow for parallelization. The open-source Python library `tomopy` (version 1.4.2)²⁸ was selected for its implementation of the *gridrec* reconstruction algorithm.²⁹ The reconstruction section of the pipeline was thus written in Python (version 3.7.4). It read a block of sinograms, took the negative logarithm, performed tomographic reconstruction with `tomopy's gridrec`, then cropped, re-scaled, and saved the reconstructed slices as a stack of TIFF images.

3. RESULTS AND DISCUSSION

3.1 Comparison of mosaic acquisition approaches

Mosaic tiling of both projections (hereafter referred to as projection tiling) and local tomography reconstructions (hereafter reconstruction tiling) have been suggested for large-volume microtomography.⁸⁻¹¹ The two approaches are illustrated in Figure 2 (note that the underlying images are from a projection-tiling acquisition), where 4 ring acquisitions are needed for projection tiling and around 50 local tomography acquisitions are needed for reconstruction tiling. The latter allows for standard reconstruction, e.g. with the PyHST2-based³⁰ software provided by the ANATOMIX beamline.^{13,14} The former requires a dedicated pipeline, as described above or by Vescovi *et al.*⁸

Angular sampling requirements for local tomography indicated that fewer projections are needed for aliasing artefact-free reconstructions^{31,32} compared with projection tiling. However, additional projections improved photon statistics, see Figure 3. Therefore, to achieve a similar signal-to-noise ratio, the number of projections for each local tomography scan must be the same as that used in each ring scan for projection tiling. With this in mind, the reconstruction tiling approach was substantially less time- and dose-efficient.

Another disadvantage of local tomography reconstruction was that the truncated sinograms must be padded to avoid cupping artefacts.¹⁸⁻²⁰ Here, local tomography scans were simulated by cropping the ring acquisition of the mouse brain around the center of rotation to produce a 2048×4495 truncated sinogram. Note that these sinograms reflected rotation about 180° . Sinograms were then padded on both sides and reconstructed, see Figure 4. To achieve artefact-free reconstructions, the truncated sinogram required padding of around 1000 pixels on both sides. More padding was likely not necessary because the sample was relatively homogenous and low absorbing at the selected photon energy of about 27 keV.

Thus, in the present case, reconstruction tiling required reconstruction of 50 sinograms of size 4048×4495 , while projection tiling required reconstruction of a single sinogram of size 14982×4495 (i.e. 3.7×1 times larger than a single padded local sinogram).

projections:

Same as ring scan

1/2

1/3

1/4

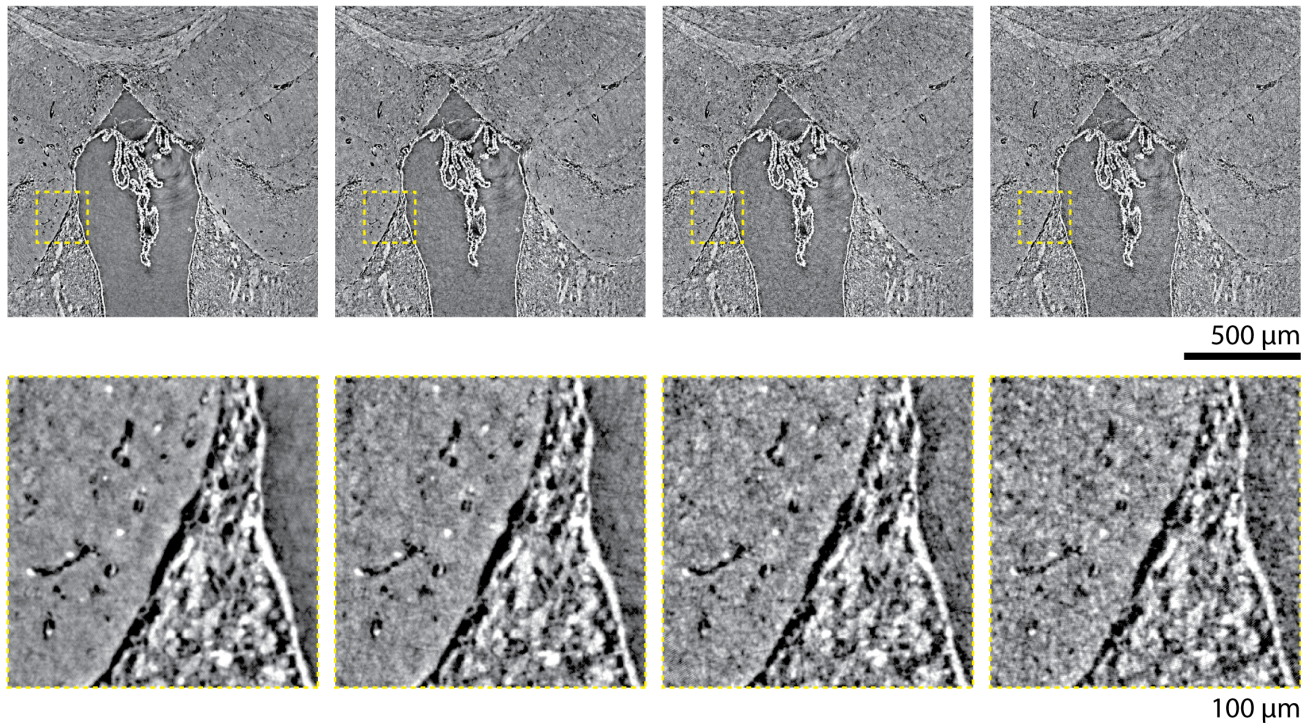


Figure 3. Angular sampling for local tomography scans. Local tomography acquisition was simulated by cropping projection-blended sinograms (14982×4495) about the center-of-rotation to produce truncated sinograms (2048×4495). Reconstructions with all 4495 projections as well as 1/2, 1/3, and 1/4 of the projections were reconstructed (left to right). While reconstructions with fewer projections did not have aliasing artefacts, the noise level increased. Magnified views are given to illustrate image quality (bottom row). Thus, local tomography acquisitions should have the same projection sampling as projection-tiling ring acquisitions to obtain equal signal-to-noise ratio. Note that truncated sinograms were padded prior to reconstruction, see Figure 4. All images were converted from $[1^{\text{st}}, 99^{\text{th}}]$ percentiles to gray values in the range of $[0, 255]$.

no padding

500 pixels

1000 pixels

3000 pixels

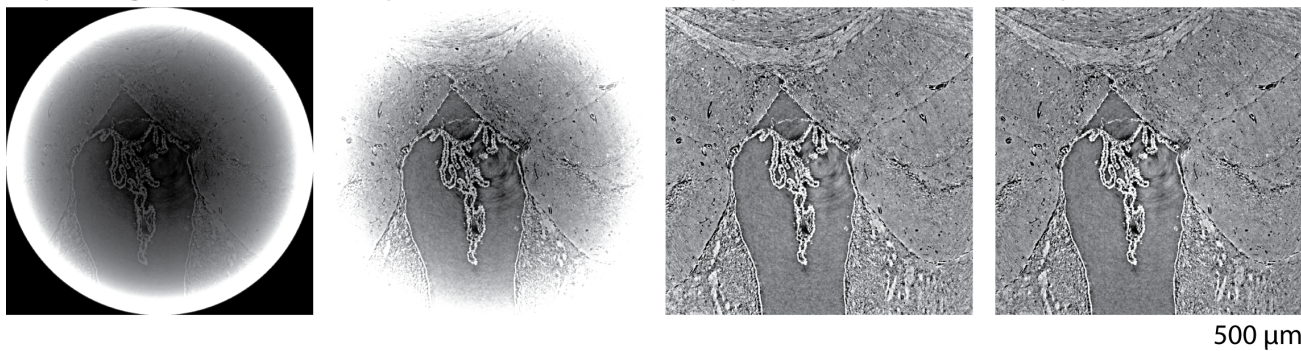


Figure 4. Padding to remove local tomography artefacts. Local tomography acquisition was simulated by cropping projection-blended sinograms (14982×4495) about the center-of-rotation to produce truncated sinograms (2048×4495). Increasing padding (left to right) removed the well-known cupping artefacts. Padding of 1000 pixels on both sides of the 2048-pixel-wide sinograms was sufficient to fully remove cupping. All images were converted from $[1^{\text{st}}, 99^{\text{th}}]$ percentiles to gray values in the range of $[0, 255]$.

3.2 Reconstruction speed for mosaic sinograms

While the first and second steps of the pipeline were written in **Matlab** (release R2020a, The MathWorks, Inc., Natick, USA), reconstruction based on **Matlab**'s built-in *filtered backprojection* algorithm (*iradon.m*) was limited for practical usage due to long reconstruction times. As a result, the open-source Python library **tomopy** (version 1.4.2)²⁸ was selected for its implementation of the *gridrec* reconstruction algorithm.²⁹ A comparison of reconstruction speeds for a single slice from a range of dataset sizes was made and the results are presented in Table 1. For reconstruction of $8\times$ extended field of view, represented in the table by 16384×16384 , **tomopy**'s *gridrec* was 60.5 times faster than **Matlab**'s *filtered backprojection*. For 2048 sinograms in one height step, this corresponds in a reduction of reconstruction time from 1111 hours (47 days) to 18.4 hours, although it should be noted that parallelization accelerates reconstruction times in both cases. Visual inspection showed no major differences in reconstruction quality between the two algorithms, see Figure 5.

Reconstruction speeds for sinograms of increasing size						
Software	Algorithm	Reconstruction time [s]				
		local 2048×2048	off-axis 4096×4096	2 rings 8192×8192	3 rings 12288×12288	4 rings 16384×16384
Matlab	<i>iradon</i>	3.7	30.0	238.6	833.8	1953.5
tomopy	<i>gridrec</i>	0.4	1.7	7.4	23.5	32.3
Speed-up factor		9.3	17.6	32.2	35.5	60.5

Table 1. Comparison of reconstruction speed with **Matlab**'s *iradon* (release R2020a), which is an implementation of a filtered backprojection, and **tomopy**'s *gridrec* (version 1.4.2). The speed-up factor represents the ratio of the former over the latter. The selected sizes represent acquisitions with increasing number of rings, ignoring overlap. A single sinogram was used with the number of projections equal to the grid width divided by 1.5, which is commonly used to avoid aliasing.³¹ Sinograms were generated by replicating or cropping the mouse brain dataset and were composed of 32 bit floating point numbers. Tabulated values are the mean of five reconstructions of the same sinogram. Note that only the reconstruction was timed and file read/write were not considered. Reconstructions were performed on a workstation with an Intel[®] Xeon[®] 16 core CPU (E5-2637 v2, 3.50GHz) and 144 GB memory.

3.3 Misalignment of overlap positions

Misaligned tiling of projections generated artefacts similar to those of misaligned center-of-rotation, as illustrated in Figure 6. Surprisingly, the mouse brain dataset was not very sensitive to misalignment in projection tiling, i.e. several pixels of misalignment were needed before cell nuclei were obscured by the artefacts. This is likely because 2 pixel spatial resolution was not achieved due to long propagation distance and application of Paganin's filter for phase retrieval.

3.4 Considerations for other samples

For the present imaging, the formalin-fixed ethanol-dehydrated mouse brain was placed in an ethanol-filled Eppendorf container. This resulted in a relatively homogenous sample with cylindrical shape. For inhomogenous samples, an alternative ring artefact correction method may be needed. In these cases, application of one or more ring artefact correction algorithms provided by the **tomopy** package²⁸ could be beneficial, for example those in Refs. 33,34.

Overlap positions were found through cross-correlation. For non-cylindrical specimens, the sample is not in the field-of-view for some projection angles, particularly for outer rings. For example, see Figure 2, where the brain is not in the field of view for parts of the outermost ring. In this case, automatic selection of projections with image content will allow for more robust calculation of overlap positions. Another potential challenge is low-contrast samples, where low-pass filtering for noise reduction and contrast enhancement may improve automatic selection of overlap positions. If an automatic approach is infeasible, a user can run a series of reconstructions over a range of overlap positions and make a selection based on minimization of artefacts, see Figure 6. Since misalignment in outer rings has minimal effect on inner rings, cf. Figure 6 top vs. bottom, overlap positions can be selected sequentially from inside to outside.

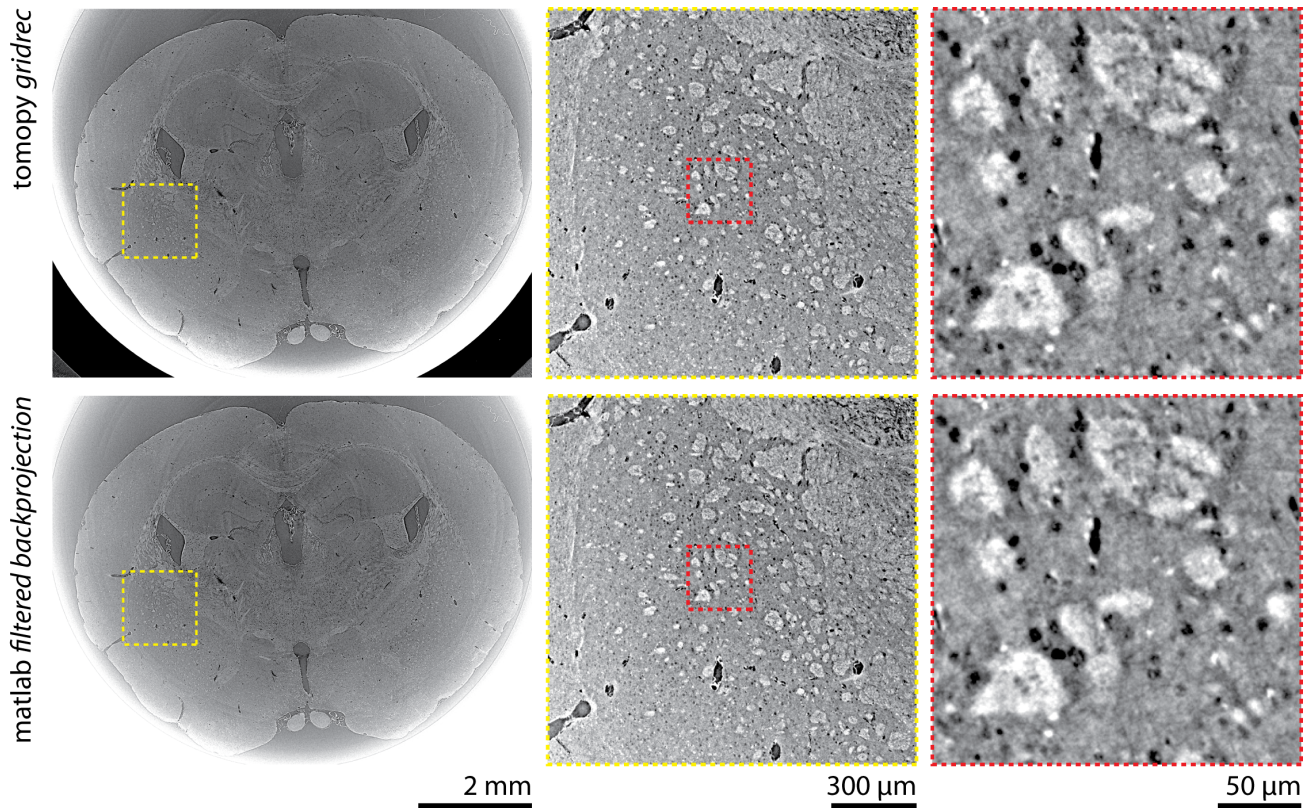


Figure 5. Comparison of reconstruction algorithms. The same 14982×4495 sinogram was reconstructed with *tomopy's gridrec* (version 1.4.2) (top) and *Matlab's filtered backprojection (iradon, release R2020a)* (bottom). The full brain coronal cross-section (left, binned 4×4) and unbinned magnified views within the caudate putamen (center, right) are shown. All images are displayed with intensities from [1st, 99th] percentiles mapped to gray values in the range of [0, 255]. Visual inspection reveals no discernible differences in image quality.

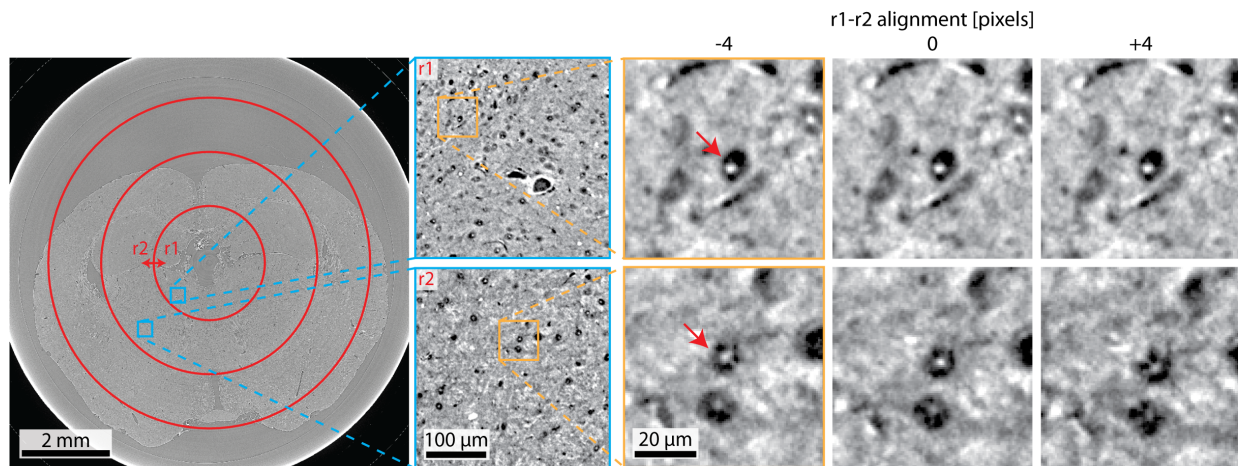


Figure 6. Artefacts due to misalignment of mosaic-tiled projections. The overlap between rings 1 and 2 (left) was set to the found position plus -4, 0, and 4 pixels. Magnified views show the resulting reconstructions (right). Misalignment is best seen for small structures with known shape, such as cells with circular nuclei (red arrow). Unsurprisingly, structures of inner rings (top row) do not show artefacts when outer rings are misaligned (bottom row).

3.4.1 The full mouse brain dataset

The full mouse brain, defined here from the top of the olfactory bulbs to the bottom of the cerebellum, was scanned with 8 height steps. The resulting stitched datasets contained $14982 \times 14982 \times 14784$ voxels, or 3.3 teravoxels. At 16-bit precision, the resulting datasets were 6.6 TB in size. It should be noted that this reflects the entire reconstructed FOV of 911 mm^3 . Cropping to more closely cover the approximately 450 mm^3 volume of the mouse brain will reduce data size.

Sub- μm pixel sizes allow for visualizing individual neurons and their morphology across the entire mouse brain. Microanatomical details within the hippocampus and thalamus are highlighted within a virtual coronal slice in Figure 7. In-plane, the data provide details similar to conventional histology; however, μCT has isotropic resolution. This allows for exploration of the dataset in any virtual slicing planes, see Figure 8. Some cupping is observed, i.e. reduced intensity towards the center of the volume, which is may be the result of beam hardening or the applied ring correction.

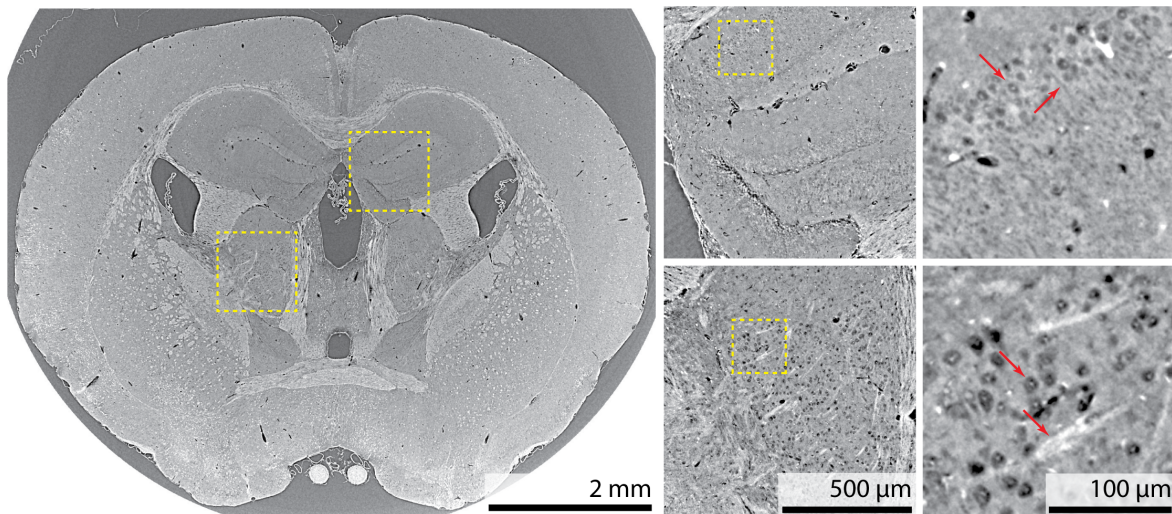


Figure 7. Microanatomical details within a virtual coronal slice. (top) Within the hippocampus, pyramidal neurons and their dendritic trees in the Ammon's horn are resolved. (bottom) Neurons and fiber tracts are shown in magnified views of the thalamus. In-plane, the data provide details similar to conventional histology; however, μCT has isotropic resolution.

3.5 Registration and segmentation of mosaic tomography data

Registration is an important tool for analysis of neuroimaging data and generation of brain atlases. Three-dimensional registration, particularly non-rigid registration, requires significant computational resources. For example, in a recent study the full mouse brain could only be non-rigidly registered after downsampling to $9.3 \mu\text{m}$ -wide voxels.^{23,35} Even then, B-spline grid spacing below 12 were not possible on a workstation with 144 GB RAM.^{23,35} These challenges could potentially be addressed with a hierarchical approach with sub-volume registration for the full resolution steps. In the next steps of this project, the data will be registered to the Allen Mouse Brain Common Coordinate Framework.³⁶

Segmentation of anatomical regions can be challenging in label-free virtual histology, thus manual approaches are used in many cases. Terabyte-sized datasets require automated segmentation approaches. In certain cases, selection of an embedding material can allow for simple semi-automatic segmentation. For example, ethanol-based contrast enhancement allows fiber tracts to be segmented with region growing from a handful of manually defined seed points in an ethanol-dehydrated mouse brain.^{22,23,37} Automatic detection of cells^{3,5} could also allow for determination of anatomical regions based on cell distributions.³⁸⁻⁴⁰ Additionally, machine-learning based approaches have shown success for terabyte-scale microtomography segmentation, for example to segment 33729 glomeruli in a mouse kidney.⁴¹

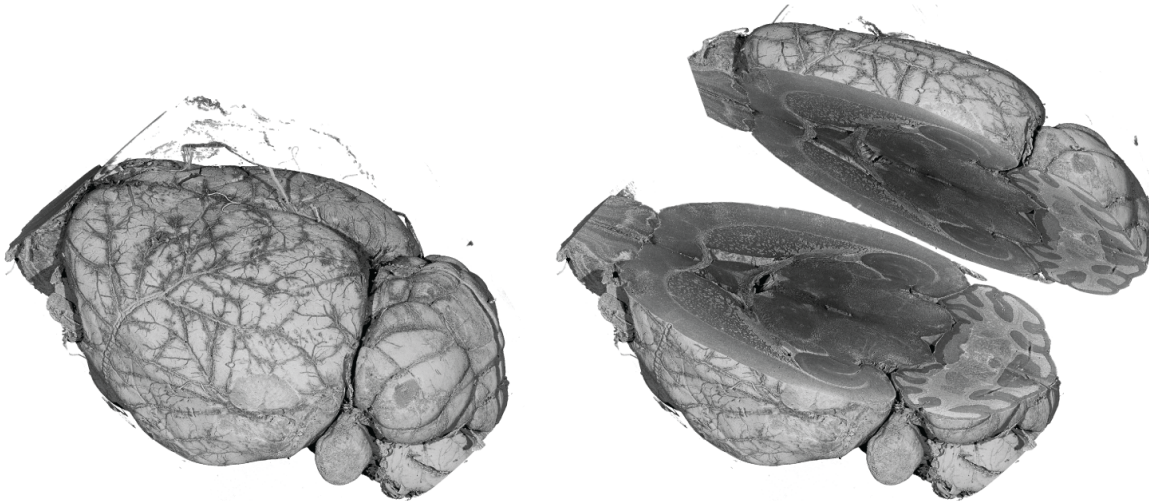


Figure 8. Volume rendering of the mouse brain dataset. Volumetric imaging with isotropic resolution allows for exploration of the brain along any virtual slicing direction, here an axial slice is shown. Note that the rendering represents $8\times$ binned data, which has a size around 10 GB and can be handled by a standard workstation. Multi-resolution approaches are necessary for these teravoxel datasets. These volume rendering were made with *VGStudio MAX 2.1* (Volume Graphics, Heidelberg, Germany).

3.6 Visualization and sharing of TB-sized data

Currently, exploration and visualization of the 6.6 TB volume have been based on a hierarchical strategy, where downsampled volumes are used to explore the full brain, then relevant regions are manually selected and loaded from the high resolution volume for closer inspection. This method can be used on a standard workstation, but is cumbersome and does not facilitate sharing. After registration to the Allen Mouse Common Coordinate Framework,³⁶ we plan to disseminate the data using *Neuroglancer*, which is an open-source browser-based interactive visualization platform that allows for datasets up to PB in size.⁴² After data is converted to a format compatible with their hierarchical viewer, it can be loaded into the viewer using a URL.

4. CONCLUSION

Extending the FOV of virtual histology is critical for brain mapping with true micrometer resolution. We present proof-of-concept imaging of an entire mouse brain with $0.65\ \mu\text{m}$ pixel size. This represents a $400\times$ increase in imaged volume compared with a single local tomography. Mosaic imaging methods were compared and a projection tiling approach was selected because of its time- and dose-efficiency. A dedicated data processing pipeline has been established for the reconstruction of these terabyte-sized datasets. These datasets will enable quantification of brain microanatomy in health and disease. Going forward, the registration and segmentation of these large datasets will be major challenges.

ACKNOWLEDGMENTS

The authors thank Dr. V. Meskenaite and J. de Tenorio of the Institute of Physiology, University of Zurich for providing excess cadavers for sample extraction. The authors thank Prof. M.D. Ruslan Hlushchuk and his team at the Institute of Anatomy, University of Bern for supplying additional mice.

Beamtime at the ANATOMIX beamline was granted by Synchrotron SOLEIL under proposals 20190424 and 20200712. ANATOMIX is an Equipment of Excellence (EQUIPEX) funded by the Investments for the Future program of the French National Research Agency (ANR), project NanoimagesX, grant no. ANR-11-EQPX-0031. V.K. acknowledges support from the Swiss National Science Foundation *via* NCCR Kidney.ch and project no. 182683. G.R., C.T., and B.M. acknowledge support from the Swiss National Science Foundation project no. 185058.

REFERENCES

- [1] Lichtman, J. W. and Denk, W., “The Big and the Small: Challenges of Imaging the Brain’s Circuits,” *Science* **334**, 618–623 (Nov. 2011).
- [2] Khimchenko, A., Deyhle, H., Schulz, G., Schweighauser, G., Hench, J., Chicherova, N., Bikis, C., Hieber, S. E., and Müller, B., “Extending two-dimensional histology into the third dimension through conventional micro computed tomography,” *NeuroImage* **139**, 26–36 (Oct. 2016).
- [3] Hieber, S. E., Bikis, C., Khimchenko, A., Schweighauser, G., Hench, J., Chicherova, N., Schulz, G., and Müller, B., “Tomographic brain imaging with nucleolar detail and automatic cell counting,” *Scientific Reports* **6**, 32156 (Sept. 2016).
- [4] Dyer, E. L., Roncal, W. G., Prasad, J. A., Fernandes, H. L., Gürsoy, D., Andrade, V. D., Fezzaa, K., Xiao, X., Vogelstein, J. T., Jacobsen, C., Körding, K. P., and Kasthuri, N., “Quantifying Mesoscale Neuroanatomy Using X-Ray Microtomography,” *eNeuro* **4** (Sept. 2017).
- [5] Töpferwien, M., van der Meer, F., Stadelmann, C., and Salditt, T., “Three-dimensional virtual histology of human cerebellum by X-ray phase-contrast tomography,” *Proceedings of the National Academy of Sciences* **115**, 6940–6945 (July 2018).
- [6] Töpferwien, M., van der Meer, F., Stadelmann, C., and Salditt, T., “Correlative x-ray phase-contrast tomography and histology of human brain tissue affected by Alzheimer’s disease,” *NeuroImage* **210**, 116523 (Apr. 2020).
- [7] Ma, Y., Hof, P. R., Grant, S. C., Blackband, S. J., Bennett, R., Slatest, L., McGuigan, M. D., and Benveniste, H., “A three-dimensional digital atlas database of the adult C57BL/6J mouse brain by magnetic resonance microscopy,” *Neuroscience* **135**, 1203–1215 (Jan. 2005).
- [8] Vescovi, R., Du, M., de Andrade, V., Scullin, W., Gürsoy, D., and Jacobsen, C., “Tomosaic: Efficient acquisition and reconstruction of teravoxel tomography data using limited-size synchrotron X-ray beams,” *Journal of Synchrotron Radiation* **25**, 1478–1489 (Sept. 2018).
- [9] Du, M., Vescovi, R., Fezzaa, K., Jacobsen, C., and Gürsoy, D., “X-ray tomography of extended objects: A comparison of data acquisition approaches,” *JOSA A* **35**, 1871–1879 (Nov. 2018).
- [10] Miettinen, A., Oikonomidis, I. V., Bonnin, A., and Stampanoni, M., “NRStitcher: Non-rigid stitching of terapixel-scale volumetric images,” *Bioinformatics* **35**, 5290–5297 (Dec. 2019).
- [11] Vo, N. T., Atwood, R. C., Drakopoulos, M., and Connolley, T., “Data processing methods and data acquisition for samples larger than the field of view in parallel-beam tomography,” *Optics Express* **29**, 17849–17874 (June 2021).
- [12] Foxley, S., Sampathkumar, V., De Andrade, V., Trinkle, S., Sorokina, A., Norwood, K., La Riviere, P., and Kasthuri, N., “Multi-modal imaging of a single mouse brain over five orders of magnitude of resolution,” *NeuroImage* **238**, 118250 (Sept. 2021).
- [13] Weitkamp, T., Scheel, M., Giorgetta, J. L., Joyet, V., Roux, V. L., Cauchon, G., Moreno, T., Polack, F., Thompson, A., and Samama, J. P., “The tomography beamlineANATOMIXat Synchrotron SOLEIL,” *Journal of Physics: Conference Series* **849**, 012037 (June 2017).
- [14] Weitkamp, T., Scheel, M., Perrin, J., Daniel, G., King, A., Roux, L., V, Giorgetta, J.-L., Carcy, A., Langlois, F., Desjardins, K., Meneglier, C., Cerato, M., Engblom, C., Cauchon, G., Moreno, T., Rivard, C., Gohon, Y., and Polack, F., “Microtomography on the ANATOMIX beamline at Synchrotron SOLEIL,” (July 2022).
- [15] Kyrieleis, A., Ibison, M., Titarenko, V., and Withers, P. J., “Image stitching strategies for tomographic imaging of large objects at high resolution at synchrotron sources,” *Nuclear Instruments and Methods in Physics Research Section A: Accelerators, Spectrometers, Detectors and Associated Equipment* **607**, 677–684 (Aug. 2009).
- [16] Miettinen, A., Oikonomidis, I. V., Bonnin, A., and Stampanoni, M., “NRStitcher: Non-rigid stitching of terapixel-scale volumetric images,” *Bioinformatics* **35**, 5290–5297 (Dec. 2019).
- [17] Vescovi, R. F. C., Cardoso, M. B., and Miqueles, E. X., “Radiography registration for mosaic tomography,” *Journal of Synchrotron Radiation* **24**, 686–694 (May 2017).
- [18] Kyrieleis, A., Titarenko, V., Ibison, M., Connolley, T., and Withers, P. J., “Region-of-interest tomography using filtered backprojection: Assessing the practical limits,” *Journal of Microscopy* **241**(1), 69–82 (2011).

- [19] da Silva, J. C., Guizar-Sicairos, M., Holler, M., Diaz, A., van Bokhoven, J. A., Bunk, O., and Menzel, A., “Quantitative region-of-interest tomography using variable field of view,” *Optics Express* **26**, 16752–16768 (June 2018).
- [20] Robisch, A.-L., Frohn, J., and Salditt, T., “Iterative micro-tomography of biopsy samples from truncated projections with quantitative gray values,” *Physics in Medicine & Biology* **65**, 235034 (Nov. 2020).
- [21] Töpferwien, M., Markus, A., Alves, F., and Salditt, T., “Contrast enhancement for visualizing neuronal cytoarchitecture by propagation-based x-ray phase-contrast tomography,” *NeuroImage* **199**, 70–80 (Oct. 2019).
- [22] Rodgers, G., Kuo, W., Schulz, G., Scheel, M., Migga, A., Bikis, C., Tanner, C., Kurtcuoglu, V., Weitkamp, T., and Müller, B., “Virtual histology of an entire mouse brain from formalin fixation to paraffin embedding. Part 1: Data acquisition, anatomical feature segmentation, tracking global volume and density changes,” *Journal of Neuroscience Methods* **364**, 109354 (Dec. 2021).
- [23] Rodgers, G., Tanner, C., Schulz, G., Migga, A., Kuo, W., Bikis, C., Scheel, M., Kurtcuoglu, V., Weitkamp, T., and Müller, B., “Virtual histology of an entire mouse brain from formalin fixation to paraffin embedding. Part 2: Volumetric strain fields and local contrast changes,” *Journal of Neuroscience Methods* **365**, 109385 (Jan. 2022).
- [24] Desjardins, K., Carcy, A., Giorgetta, J.-L., Meneglier, C., Scheel, M., and Weitkamp, T., “Design of Indirect X-Ray Detectors for Tomography on the Anatomix Beamline,” in [*Mechanical Eng. Design of Synchrotron Radiation Equipment and Instrumentation (MEDSI’18), Paris, France, 25-29 June 2018*], 355–357, JACOW Publishing, Geneva, Switzerland (Dec. 2018).
- [25] Weitkamp, T., Haas, D., Wegrzynek, D., and Rack, A., “ANKAphase: Software for single-distance phase retrieval from inline X-ray phase-contrast radiographs,” *Journal of Synchrotron Radiation* **18**, 617–629 (July 2011).
- [26] Paganin, D., Mayo, S. C., Gureyev, T. E., Miller, P. R., and Wilkins, S. W., “Simultaneous phase and amplitude extraction from a single defocused image of a homogeneous object,” *Journal of Microscopy* **206**(1), 33–40 (2002).
- [27] Rodgers, G., Schulz, G., Deyhle, H., Kuo, W., Rau, C., Weitkamp, T., and Müller, B., “Optimizing contrast and spatial resolution in hard x-ray tomography of medically relevant tissues,” *Applied Physics Letters* **116**, 023702 (Jan. 2020).
- [28] Gürsoy, D., De Carlo, F., Xiao, X., and Jacobsen, C., “TomoPy: A framework for the analysis of synchrotron tomographic data,” *Journal of Synchrotron Radiation* **21**, 1188–1193 (Sept. 2014).
- [29] Marone, F. and Stampanoni, M., “Regridding reconstruction algorithm for real-time tomographic imaging,” *Journal of Synchrotron Radiation* **19**, 1029–1037 (Nov. 2012).
- [30] Mirone, A., Brun, E., Gouillart, E., Tafforeau, P., and Kieffer, J., “The PyHST2 hybrid distributed code for high speed tomographic reconstruction with iterative reconstruction and a priori knowledge capabilities,” *Nuclear Instruments and Methods in Physics Research Section B: Beam Interactions with Materials and Atoms* **324**, 41–48 (Apr. 2014).
- [31] Kak, A. C. and Slaney, M., [*Principles of Computerized Tomographic Imaging*], Classics in Applied Mathematics, Society for Industrial and Applied Mathematics (Jan. 2001).
- [32] Stock, S. R., [*MicroComputed Tomography: Methodology and Applications*], CRC Press, Boca Raton (Oct. 2018).
- [33] Münch, B., Trtik, P., Marone, F., and Stampanoni, M., “Stripe and ring artifact removal with combined wavelet — Fourier filtering,” *Optics Express* **17**, 8567–8591 (May 2009).
- [34] Vo, N. T., Atwood, R. C., and Drakopoulos, M., “Superior techniques for eliminating ring artifacts in X-ray micro-tomography,” *Optics Express* **26**, 28396–28412 (Oct. 2018).
- [35] Rodgers, G., Schulz, G., Kuo, W., Scheel, M., Kurtcuoglu, V., Weitkamp, T., Müller, B., and Tanner, C., “Non-rigid registration to determine strain fields during mouse brain fixation and embedding,” in [*Bioinspiration, Biomimetics, and Bioreplication XI*], **11586**, 115860I, International Society for Optics and Photonics (Mar. 2021).

- [36] Wang, Q., Ding, S.-L., Li, Y., Royall, J., Feng, D., Lesnar, P., Graddis, N., Naeemi, M., Facer, B., Ho, A., Dolbeare, T., Blanchard, B., Dee, N., Wakeman, W., Hirokawa, K. E., Szafer, A., Sunkin, S. M., Oh, S. W., Bernard, A., Phillips, J. W., Hawrylycz, M., Koch, C., Zeng, H., Harris, J. A., and Ng, L., “The Allen Mouse Brain Common Coordinate Framework: A 3D Reference Atlas,” *Cell* **181**, 936–953.e20 (May 2020).
- [37] Rodgers, G., Tanner, C., Schulz, G., Migga, A., Weitkamp, T., Kuo, W., Scheel, M., Osterwalder, M., Kurtcuoglu, V., and Müller, B., “Impact of fixation and paraffin embedding on mouse brain morphology: A synchrotron radiation-based tomography study,” in [*Developments in X-Ray Tomography XIII*], **11840**, 118400P, International Society for Optics and Photonics (Aug. 2021).
- [38] LaGrow, T. J., Moore, M. G., Prasad, J. A., Davenport, M. A., and Dyer, E. L., “Approximating Cellular Densities from High-Resolution Neuroanatomical Imaging Data,” in [*2018 40th Annual International Conference of the IEEE Engineering in Medicine and Biology Society (EMBC)*], 1–4, IEEE, Honolulu, HI (July 2018).
- [39] Prasad, J. A., Balwani, A. H., Johnson, E. C., Miano, J. D., Sampathkumar, V., De Andrade, V., Fezzaa, K., Du, M., Vescovi, R., Jacobsen, C., Kording, K. P., Gürsoy, D., Gray Roncal, W., Kasthuri, N., and Dyer, E. L., “A three-dimensional thalamocortical dataset for characterizing brain heterogeneity,” *Scientific Data* **7**, 358 (Oct. 2020).
- [40] Balwani, A., Miano, J., Liu, R., Kitchell, L., Prasad, J. A., Johnson, E. C., Gray-Roncal, W., and Dyer, E. L., “Multi-Scale Modeling of Neural Structure in X-Ray Imagery,” in [*2021 IEEE International Conference on Image Processing (ICIP)*], 141–145 (Sept. 2021).
- [41] Kuo, W., Rossinelli, D., Schulz, G., Wenger, R. H., Hieber, S., Müller, B., and Kurtcuoglu, V., “Terabyte-scale supervised 3D training and benchmarking dataset of the mouse kidney,” *arXiv:2108.02226 [physics, q-bio]* (Aug. 2021).
- [42] Maitin-Shepard, J., Baden, A., Silversmith, W., Perlman, E., Collman, F., Blakely, T., Funke, J., Jordan, C., Falk, B., Kemnitz, N., tingzhao, Roat, C., Castro, M., Jagannathan, S., moenigin, Clements, J., Hoag, A., Katz, B., Parsons, D., Wu, J., Kamentsky, L., Chervakov, P., Hubbard, P., Berg, S., Hoffer, J., Halageri, A., Machacek, C., Mader, K., Roeder, L., and Li, P. H., “google/neuroglancer:,” (Oct. 2021). v2.23, <https://doi.org/10.5281/zenodo.5573294>.